

A Planet as the Possible Cause of the HD 181327 Debris Disk Asymmetry

Chris Fox^{1,2*}, Paul Wiegert^{1,2}

¹*Department of Physics & Astronomy, The University of Western Ontario, London, Ontario, Canada*

²*Institute for Earth and Space Exploration (IESX), The University of Western Ontario, London, Ontario, Canada*

Submitted to the Monthly Notices of the Royal Astronomical Society, December 2024

ABSTRACT

The debris disk around HD 181327 shows a significant asymmetry in its surface brightness profile when viewed in visible light. Observations from the Hubble Space Telescope STIS instrument show an arc of approximately 90° of higher optical depth at a distance of 84 au from the star. We find that a 2-5 Jupiter-mass planet on a circular orbit at 62 au can produce and maintain a similar feature if the collisional lifetime of dust in the disk is at least 25 kiloyears, and smaller mass planets can produce similar results on longer timescales. We also find that the surface brightness asymmetry is much less pronounced at larger particle sizes, which may account for the fact that observations of HD181327 at longer wavelengths have not reported such an arc. We predict that if a planet is producing the arc in question, the planet is along the line joining the star to the feature, and make some estimates of its observability.

Key words: planets and satellites: detection, methods: numerical, stars: individual: HD 181327

1 INTRODUCTION

HD 181327 (also known as HIP 95270) is an 18.5 Myr old main sequence F5/6 star in the Beta Pictoris Moving Group (Milli, J. et al. 2024; Miret-Roig et al. 2020). Its debris disk was discovered by Schneider et al. (2006) in the near-infrared, and the disk has been the target of many further observations since. Lebreton et al. (2012) examined it in the far-infrared and found an icy Kuiper belt. Marino et al. (2016) reported the presence of exocometary gas in the disk. More recently, Milli, J. et al. (2024) examined polarization properties of the disk and found evidence for sub-micron particles.

Most relevant to our work here, Stark et al. (2014) observed the disk with the Space Telescope Imaging Spectrograph (STIS) on board the Hubble Space Telescope. They found a debris disk with optical depth peaking at 84.2 au. When deprojected, the disk showed a significant azimuthal asymmetry manifesting as a 90° arc of increased optical depth. In that work, the asymmetry was interpreted as a region of higher particle density, and the cause hypothesized as warping due to interaction with the interstellar medium or the result of a catastrophic disruption of a 1% Pluto-mass object within an exo-Kuiper belt. In a related work, Schneider et al. (2014) suggested the asymmetry may indicate the presence of unseen planetary companions.

It has long been recognized that debris disks may host unseen planets (Wyatt et al. 1999) and that planets may produce observable disk structures while the planets themselves may remain unobserved (Mouillet et al. 1997; Augereau et al. 2001; Kraus et al. 2013; Tabeshian & Wiegert 2016, 2017, 2018).

Could the visible asymmetry of the debris disk of HD 181327 be created by a gravitationally perturbing planet? Here we explore this premise through the use of N-body simulations of a hypothetical planet on the inner edge of the HD 181327 disk and characterize the orbital parameters of such a planet.

2 METHODOLOGY

The primary goal of this paper is to determine whether the presence of a planet near the inner edge of the HD 181327 disk provides a plausible explanation for the structures observed by Stark et al. (2014). In that paper, raw STIS observations were deprojected to produce a face-on map of the normalized optical density, resulting in Figure 6h from that paper. That map of optical density serves as the basis for our work, where we use a Bayesian search coupled iteratively with a numerical integrator to find the planetary parameters that produce a disk that most closely matches the observations. Details of this process are discussed in the following sub-sections.

2.1 Update of Distance Values

Stark et al. (2014) reported the peak of the HD 181327 ring at a distance of 90.5 au from the central star. That work (and several others) use a distance for the system of 51.8 pc. However, updated values from Gaia put the stellar distance of HD 181327 at 48.2 pc (Gaia Collaboration et al. 2018), and our work will be performed using that value. Rescaling Stark’s distance with the newer distance estimate results in a ring radius of 84.2 au. We scale all of Stark’s (and other sources) distance values throughout this paper accordingly.

2.2 Creating the Target Map

Our first step was to adapt Figure 6h of Stark et al. (2014) to our purposes. This is the deprojected, normalized, optical depth map of the STIS image. We extracted a subset of the Stark et al. original map, sized to cover the majority of the disk but excluding the faint edges well beyond the visible asymmetries. This corresponds to an outer radius of 150 au. Our resulting map extends is 89×89 pixels, with each pixel being equivalent to 3.646 au across.

Early in our analysis, we noted that in all cases that the disk after

* Contact e-mail: cfox53@uwo.ca

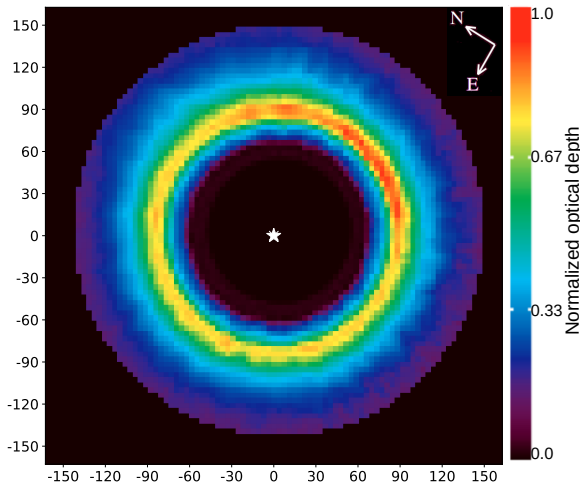


Figure 1. Our revised Target Map of HD 181327, used for all comparisons in our simulations. This is based on the original from [Stark et al. \(2014\)](#), but with the disk shifted to the west (up on pixel and to the right one pixel) for reasons described in Section 2.2, and with data outside of 150 au removed. This is the map our simulations aim to replicate via the influence of a shepherding planet. The arc is near-centred on the western side.

being carved by the planet was slightly elliptical. Closer inspection revealed that simulated disks that included a planet with a mass of a few M_J had an eccentricity of ≈ 0.04 , which is slightly higher than the deprojected value of 0.02 ± 0.01 (on the inner edge) reported by [Stark et al. \(2014\)](#). Thus if a planet is the cause of the observed asymmetry, the star is likely not at the precise centre of the disk but offset by approximately one pixel. This difference could not be expected to be measurable in the HST STIS images, and could easily be accounted for by the challenging processing associated with masking out the central star. To account for this offset, the map was shifted slightly to the west, one pixel up and one pixel to the right, for our comparisons. Our revised map, adapted from the original Figure 6h from Stark, is seen in Figure 1 where we have adopted the same colour scale as Stark et al. Henceforth, we refer to this as "Target Map" or "Target Disk", which we aim to replicate via our simulations.

2.3 Simulation Initial Conditions

2.3.1 Dust grain sizes

Our simulations examine particles of different sizes, their dynamics being characterized by β , the ratio of the force from stellar radiation to the star's gravitational force. β may be expressed as ([Wyatt & Whipple 1950](#)):

$$\beta = \frac{F_{rad}}{F_{grav}} = \frac{3L_{\odot}Q_{pr}}{16\pi GM_{\odot}c\rho r} \quad (1)$$

where c is the speed of light, G is the gravitational constant, L_{\odot} is the luminosity of the Sun, and Q_{pr} is the radiation pressure coefficient. For the Sun, β simplifies to $0.285/r$ (assuming $Q_{pr}=1$ and $\rho=2 \text{ g/cm}^3$), where r is the particle's radius in microns. For HD 181327, the star is 1.36 times more massive and 3.33 times more luminous than the Sun ([Lebreton et al. 2012](#)), so Equation 1 becomes $\beta = 1.396/\rho r$ for HD 181327, where we include ρ (in g/cm^3) to account for possible grain densities differences.

[Lebreton et al. \(2012\)](#) modeled the composition of the HD 181327 disk and found the best fit minimum grain size of $0.9 \mu\text{m}$. [Milli, J. et al. \(2024\)](#) also found evidence for sub-micron grains. STIS has a central

bandpass of $0.585 \mu\text{m}$ with a FWHM of $0.441 \mu\text{m}$ ([Medallon et al. 2023](#)). The best model from [Lebreton et al. \(2012\)](#) consisted of a disk composed of porous amorphous silicates and carbonaceous material and ice, suggesting low density ($< 1 \text{ g/cm}^3$) particles. However, more recently [Milli, J. et al. \(2024\)](#) found that their observations required a more refracting component such as iron-bearing material, which would have a significantly higher density.

For this paper, we are only concerned with the dynamical behaviour of the particles, not their exact composition or sizes. For convenience we assume a mean density of 2 g/cm^3 , similar to our own solar system. With this density, our range of examined β values from 0.05 to 0.8 would correspond to a physical radius range of 14 to $0.8 \mu\text{m}$ respectively, which are effective light scatterers at STIS wavelengths ($Q_{pr} \approx 1$) ([van de Hulst 1957](#)). Even if our assumed typical grain density is $4\times$ too low, the particles for this range of β would still be effective scatterers in optical wavelengths.

2.3.2 Particle radial distribution

Our simulated disk presumes that the dust grains observed in the HST STIS images are created from an unseen underlying population of planetesimals in its exoKuiper Belt. We assume grains are released from their parent bodies with an initial distribution characterized by a single unbroken power law with surface density $\Sigma(r) \propto a^{-\gamma}$, with a being the distance from the star. Because our model only examines a planet located inside the ring, we do not expect the planet to have a strong effect on the particle distribution along its outer edge. As a result, we expect that values of γ in the region just beyond the peak (90-140 au) will be largely unchanged by the planet, and remain near the value of 3.7 measured by Stark et al. for this region. We note that [Stark et al. \(2014\)](#) examined the disk as far out as 230 au and found $\gamma=1.7$ in the outermost regions, but our simulations have particle numbers that are too low to efficiently model this region. Thus, our disk is limited to particles no further out than 150 au.

We experimented with γ values between 2.0 and 4.0 and found that distributing the particles with an initial $\gamma=3.25$ produced the best fit. We'll see that our model can effectively explain the dust distribution in the densest part of the ring, but does not have much to say about the distribution beyond 140 au. Our initial particle distribution is shown in Figure 2.

2.3.3 Eccentricity and β distribution

We examined a number of different scenarios for the dust particle eccentricities. One class of scenarios assumed that all particles were created in the primary region (84 ± 20 au) with particles on high eccentricity orbits which subsequently moved out into and populated the extended disk. However, such simulations were not able to produce patterns anything like the Target Map. Most particles on such high eccentricity orbits have little interaction with the planet, and thus can not be driven into the requisite regions on the short timescales required by the expected collision lifetimes (see Section 2.5).

The other class of scenarios, in which we are able to produce reasonable matches to our Target Disk, presume grains are created throughout the disk and are released onto initially low eccentricity orbits. In the discussion below, we restrict ourselves to particle distributions with $e \leq 0.1$, inclinations of 0° , and the other angular orbital elements chosen uniformly at random.

The release of dust grains with substantial β values from parent bodies on circular orbits can result in particles that are immediately on more eccentric orbits and even on unbound trajectories, as the

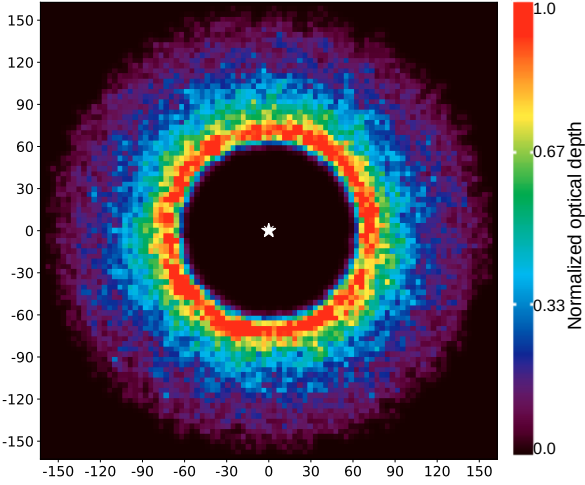


Figure 2. Our starting disk, representing the distribution of particle creation. The particles have random eccentricities from 0.0 to 0.1, and semimajor axes of 65 au to 150 au. The particle density profile is proportional to $r^{-3.25}$.

effect of radiation pressure from the star decreases that central body’s effective gravity. We will find that our simulations produce the best match to the Target Disk when a substantial component of the dust has large ($\beta \approx 0.5$). Particles with $\beta > 0.5$ are often assumed to be quickly lost from the system (“beyond the blow-out threshold”) because a particle with $\beta > 0.5$ released at zero speed from a parent body on a circular orbit will immediately find itself on an unbound orbit and leave the system. However, particles with $\beta > 0.5$ can remain comfortably bound to the star; the precise orbit of an ejected dust grain depends sensitively on the ejection velocity and direction.

If the ejection process is roughly isotropic in direction and can release particles at speeds comparable to the orbital speed, then — while many particles may quickly depart on unbound orbits— a subset of the grains released will be put into bound low-eccentricity orbits. For the case of HD 181327, the speeds needed are on the order of 1 km/s relative to the parent body. Such speeds are consistent with ejecta from asteroid collisions (Jutzi et al. 2019). Many particles produced in collisions will be put on escape trajectories, and these will leave the system in timescales of a few hundred years. Only those that are put into bound orbits will remain to contribute significantly to the final observed disk. Thus, our hypothesized model where a planet produces the HD 181327 disk asymmetry requires the continuous replenishment of dust by a process that produces relatively high ejection speeds such as the continuous collisional grinding of the underlying planetesimal population, while processes with low ejection speeds such as traditional cometary activity are disfavoured.

2.3.4 Particle count and stacking

Our simulated disk begins with 9600 particles. During the simulations, snapshots of the disk are taken at 20 evenly spaced time intervals throughout the simulation, which are then stacked together. The length of the simulation thus corresponds to the collisional lifetime of the dust and includes particles of a range of ages; for simplicity we assume that all the dust survives for the entire simulation and is destroyed at the end. The stacked snapshots thus represent the quasi-equilibrium state resulting from the continual creation, evolution and destruction of particles through their lifetime. The number of particles used in the final comparison could be as high as

9600×21=201600, but in most cases about 25% of the particles are lost during the evolution (see Sections 2.4 and 2.5).

2.4 Running the Simulations: Numerical Integrator

The numerical integrator we use for modeling the disk is based on the Wisdom-Holman fast symplectic integration scheme (Wisdom & Holman 1991), with a time step of 500 days. This time step is approximately 1% of the planet’s period when its semimajor axis is 30 au (the lower limit of the prior, Section 2.7). This allows for adequate sampling of all particles throughout their orbit regardless of the planetary semimajor axis chosen. Only planets interior to the disk are considered. Radiation pressure and Poynting-Robertson drag are included for particles with $\beta > 0$. Particles are removed from the simulation if they move inside 15 au or outside 300 au. The duration of our simulations depended upon the expected collisional lifetime of the particles, described in the next section.

2.5 Simulation Duration / Particle Lifetimes

The simulated disk is strongly affected by the adopted collisional timescale of the particles, as the particles have only this amount of time to respond to the presence of the planet and develop any resulting structures.

We can estimate the collisional lifetime of the HD 181327 disk from the particle density as determined by the amount of light received at Earth. The surface brightness of a pixel in terms of power received by Hubble’s STIS instrument is:

$$P_H = A_H \frac{L_p}{4\pi D^2} \quad (2)$$

where A_H is the collecting area of Hubble’s primary mirror (4 m²), L_p is the power reflected by the dust in that pixel, and D is the distance to the star (48.2 pc). The raw STIS data from Stark et al. (2014) (Figure 1 of that paper) has a pixel width of $S = 2.446$ au (this is adjusted from the original Stark value, using the updated Gaia distance), a peak value of 6 counts, and a CCD Gain of 4 (Schneider et al. 2014). Assuming an average photon wavelength of 0.585 μ m, the central bandpass of STIS (Medallon et al. 2023), we estimate the peak power received at Hubble from one pixel as 8.15×10^{-18} W.

The power reflected by one dust grain is:

$$L_{grain} = \alpha \pi r^2 \frac{L_*}{4\pi a^2} \quad (3)$$

where L_* is the luminosity of the star, α is the albedo of the dust particle, a is the distance of the particle from the star and r is the radius of the dust particle. Lebreton et al. (2012) puts the observed albedo at 0.13 which we will adopt here though this is at 1.1 μ m, slightly above the upper wavelength limit of STIS.

Combining Equations 2 and 3 we can derive the number N of particles inside of one image pixel as:

$$N = \frac{16\pi D^2 a^2 P_H}{\alpha L_* A_H r^2} \quad (4)$$

The surface density is the number of particles in a square pixel (width $S=2.446$ au) divided by its area. The vertical optical depth τ (surface density \times particle cross-sectional area) can be expressed as:

$$\tau = \frac{16\pi^2 D^2 a^2 P_H}{\alpha L_* A_H S^2} = 0.005 \left(\frac{\alpha}{0.13}\right)^{-1} \left(\frac{D}{48.2 \text{ pc}}\right)^2 \quad (5)$$

This gives us an estimated peak optical depth of $\tau = 0.005$, which

confirms that we are dealing with an optically thin disk. Note that in Equation 5 there is no dependence on particle size.

We now seek to estimate the collisional lifetime of a particle. From Equation 5, we estimate a particle volume density by assuming a disk scale height of 6 au (Schneider et al. 2006; Stark et al. 2014; Milli, J. et al. 2024), and then compute a mean free path of 3.5×10^{11} km. Combining typical orbital distance (~ 84.2 au), inclination ($6 \text{ au} / 84.2 \text{ au} \approx 4^\circ$) and eccentricity (~ 0.05), the typical relative speed between particles is ~ 180 m/s, which will sweep out the mean free path in ~ 60 kyr. This represents the typical lifespan of a particle in the most dense region (normalized optical depth ≈ 1). Particles outside of this narrow region can be expected to live longer. Note this is again independent of the particle size.

We note that the literature contains various formulae for collisional lifetimes of the smallest particles, and estimates for particle lifetimes vary significantly. Formulae based on the angular velocity and optical depth, $t_{coll} = (\Omega\tau)^{-1}$, are frequently used to estimate the lifetime of the smallest particles (Wyatt et al. 1999; Thébaud & Augereau 2007; Lebreton et al. 2012) and produce collision times for HD 181327 from as low as 7600 years to 20 kyr. However, numerical model-derived lifetimes indicate particles smaller than 0.1 mm in a typical disk can have longer lifetimes by multiple orders of magnitude (Thébaud & Augereau 2007), potentially up to ~ 1 Myr. An empirically derived formula, Equation 7 of Thébaud & Augereau (2007), predicts a minimum lifetime when particle size is $\sim 10\times$ the blowout size, corresponding to $\sim 14\mu\text{m}$ for our disk, and a lifetime of only 400 years. But at the blowout size, the same equation computes a lifetime of 42 kyr, with smaller particles living for significantly longer. Hence, given on the complexities in computing particle lifetimes and our own simplifications, our simulations were performed over a wide range of particle lifespans: as short as 12 kyr and as long as 200 kyr.

2.6 Conversion of Simulated Particle Surface Density to Optical Depth Map

Our Target Map is an 89×89 grid of normalized optical depth values, while our simulation is comprised of individual particles, as many as 201600 (see Section 2.4). The disk of HD 181327 has been determined to be optically thin (Schneider et al. 2006; Lebreton et al. 2012), so the surface density of our simulated particle disk is simply linearly related to the optical depth of the disk. We scale the optical depth of our simulated disks so that the total optical depth of all the pixels in the simulated disk is equal to the sum of the optical depths of all the pixels in the Target Disk.

For a fair comparison, each simulation is rescaled according to the number of particles remaining at the end of the simulation, not simply the number initialized at the beginning. For example, if in one simulation half the particles are lost by the end of the simulation, then each remaining particle has to account for twice the optical depth. Section 2.3.3 describes the precise details of the disk morphology used in the simulations.

2.7 Comparing Simulated Disks to the Target Disk: a Bayesian Search

To find the planetary parameters that best reproduce the Target Disk, we used MultiNest, a Bayesian Inference Tool (Feroz et al. 2009), coupled with our numerical integrator (Section 2.4). We restrict our MultiNest search to two parameters: the semimajor axis of the planet (assumed to be on a circular orbit) and its mass. We assume uniform

priors for both parameters. For the mass, the prior extends from 0.1 to 6.0 M_J masses, based on the work of Wahhaj et al. (2013) that constrained the minimum detectable mass. For the semimajor axis, the prior is 30 to 80 au; the inner chosen so it is inside the limit set by Rodigas et al. (2014), and the outer limit chosen so that it overlaps the inner edge of the Target Disk. MultiNest chooses the parameters from the prior, which are then fed into the numerical integrator. The simulation is run and the particles at different timesteps are collected (see below). The combined disk particles are converted to a grid of 89×89 optical densities with the total optical depth scaled to the Target Disk total (see Section 2.6). MultiNest then compares this map to the Target Disk values. For quality of comparison, we used the log-likelihood, based on the usual χ^2 metric.

$$\ln L = \sum_{i=0}^N \left(\left(\ln \frac{1}{\sigma_i \sqrt{2\pi}} \right) - \frac{(x_i - \mu_i)^2}{2\sigma_i^2} \right) \quad (6)$$

In Equation 6 x_i is the simulated optical depth, μ_i is the observed optical depth, and σ_i is the error in the observed optical depth, which we set to 0.1. The log-likelihood is computed for each pixel with orbital distance from 60 au to 140 au over the entire disk.

Each simulation is run for an amount of time representing the typical collisional lifespan of the particles: we examined lifespans of 12 kyr to 200 kyr (see Section 2.5). In our model we assume that the particles observed in reflected light are created continuously from an underlying population of larger planetesimals. To represent the continual evolution of these particles from creation (at 0 kyr) to collisional destruction, 21 snapshots taken at equal intervals of time of the disk's evolution are stacked together. In this way, a steady-state disk is achieved which includes particles of all ages from creation to destruction. However, for simplicity we do not model the time-dependence of the collisional removal, and all particles of all ages count for the same weight in our optical depth maps.

A typical single MultiNest search takes 3-4 days to complete running in parallel on a machine with 48 Intel(R) Xeon Silver 4214 CPUs. Owing to the lengthy nature of the search we chose not to add additional parameters to the MultiNest search. The effect of other parameters, such as the disk power law exponent (γ , Section 2.3.2) and the collisional lifetime of particles (Section 2.5) on the resulting disk was determined through a qualitative exploration of the possible values. Since our purpose is only to show that a planet can plausibly explain the structure seen in HD 181327 and not necessarily to determine that planet's parameters with high precision, this approach is sufficient to achieve our goal.

3 RESULTS AND ANALYSIS

3.1 Initial Observations and Particle Segmentation

Initially we examined a range of particles with $\beta = 0.05$ to 0.8. As part of our initial analysis, we divided the particles into different β ranges to see how behaviour differed, if at all. We found that only a subset of particles, those with $\beta \sim 0.5$, were able to quickly produce an arc. Away from this value, the grains were either so small that we would not expect them to be visible to STIS (Section 2.3.1), or at the larger sizes, they were found not to be driven into an arc of high density. As discussed in Section 2.3.3 particles with $\beta \approx 0.5$, despite being at or above the notional blowout limit, can persist in the disk in stable orbits depending on their relative ejection speed from their source body. We therefore focused our efforts on particles of $\beta = 0.4$ to 0.6, and the most successful results in the following sections used such particles in the simulations.

3.2 Best-Fit Results

We found that models with $0.4 < \beta < 0.6$ and a range of collisional timescales were able to closely approximate the disk observed by Stark et al. (2014). The posteriors and best-fit results for each timescale can be seen in Table 1 and figures for some representative cases are included below.

The shortest collisional lifespan we examined was 12 kyr. In this case, the main body of the primary ring has formed (normalized optical depth ≈ 0.7), but the disk remains symmetric; there has not been sufficient time to form the higher-density asymmetric arc. With a 16 kyr lifespan, the arc is visible but faint, as seen in Figure 3. With a 25 kyr lifespan, there is sufficient time to form a clearly visible arc, but still has not reached the densities of the Target Map. We conclude that if a planet is the cause of the asymmetry, particle lifetimes must be at least 25 kyr.

Every model with particle lifetimes of 25 kyr and higher is capable of producing a noticeable arc of increased density similar to that of Stark et al. (2014), though some provide better fits than others. Examples of these are seen in Figures 4 and 5, for particle lifespans of 60 kyr and 150 kyr respectively. The intensity of the arc increases with longer lifetimes.

Table 1 summarizes the results found for each lifespan. The quality of match to the Target Disk is given by the average χ^2 of the pixels taken over the entire disk. The single best overall fit occurred at a lifetime of 40 kyr, but we get very similar values for all particle lifetimes from 25 kyr to 200 kyr.

Every simulation shows a slight overall asymmetry outside of the arc: a slight over-density on one side of the disk and under-density on the other. However, these differences are small, with an average difference in optical depth of 0.036 ± 0.01 for all particle lifetimes. The maximum difference across the entire disk shows greater variation across the different lifetimes (see Table 1), and is typically ~ 0.17 .

3.3 Simulated Disk Profile

To further assess the quality of fit, we examined the cross-sectional profile of the best-fit simulated disk to compare to that observed by Stark. Figure 6 shows the normalized mean optical depth profile of the disk averaged over the entire disk. The inner edge slope rise is proportional to $a^{6.3}$ and the falloff from peak is proportional to $a^{-3.4}$. These values are very similar to those found by Stark et al. (2014) in their Figure 9, with values of 6.8 and -3.7 respectively (rescaled and re-fitted after adjustment for updated Gaia distance). The slope of the outer disk is largely influenced by our choice of γ ($a^{-3.25}$ after experimentation per Section 2.3.2) when the disk is initialized, but the inner edge slope is set entirely by the dynamics and the good match with the observed profile solidifies our confidence in this scenario.

3.4 Mass, Semimajor Axis, & Lifetime Trends

While the orbital distance of our hypothesized planet (≈ 62 au) is not sensitive to a specific particle lifetime, the required planetary mass decreases with longer lifetimes. The consistent semimajor axis suggests that a resonance may be at work. Particles of $\beta \approx 0.5$ at $a = 84.2$ au will have an orbital period of about 937 years, while the planet at ≈ 62 au has a period of 419 years. This is about a 2.2:1 period ratio, suggesting that the 2:1 mean motion resonance might be at work here, and which has been observed to be associated with structures in particle disks before (Tabeshian & Wiegert 2016).

Figure 7 shows the relationship between the posterior planet mass

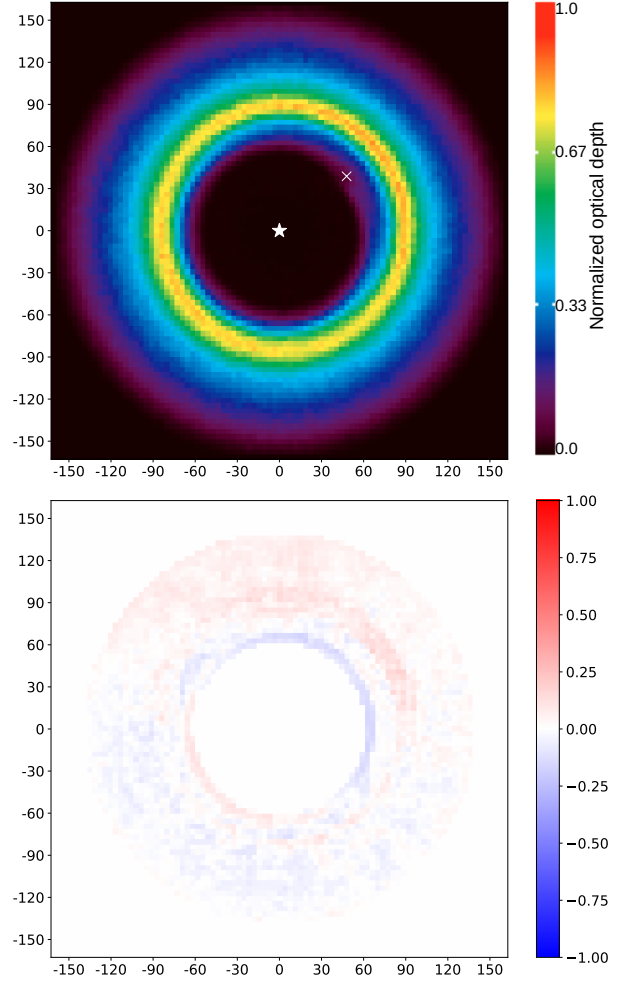


Figure 3. Best Fit result for a particle lifespan of 16 kyr. The top image is the optical depth map, while the bottom is the difference map (target values minus simulated values). The arc of higher density in the upper right quadrant is only just beginning to become apparent.

and the lifetime of the particles. The posterior mass required to generate the arc falls off with increasing lifetime, $t^{-0.2}$. As the timescale increases the importance of the mass decreases, as indicated by the larger error estimates. When we look at the best-fit masses, the slope is even steeper, proportional to the $t^{-0.3}$

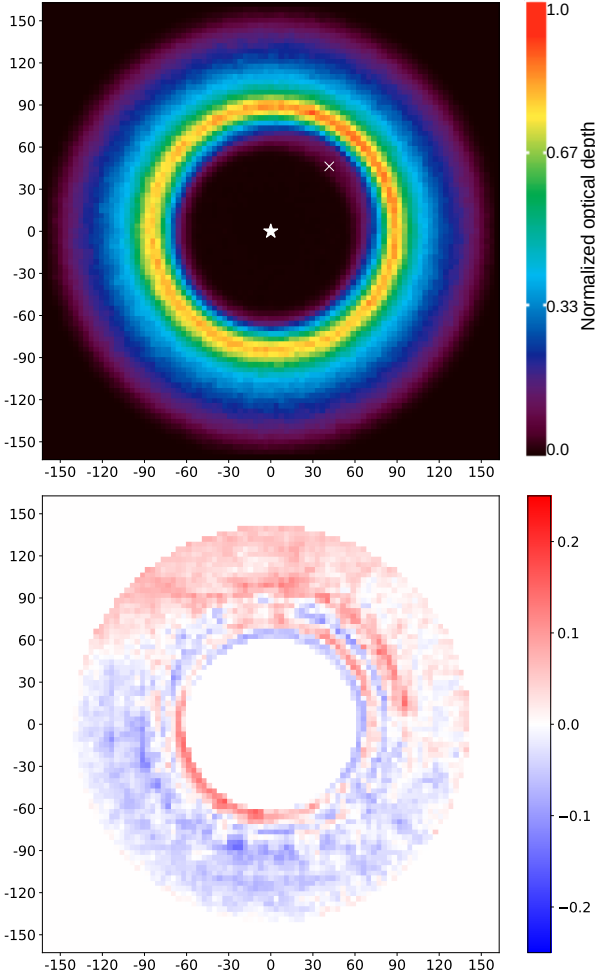
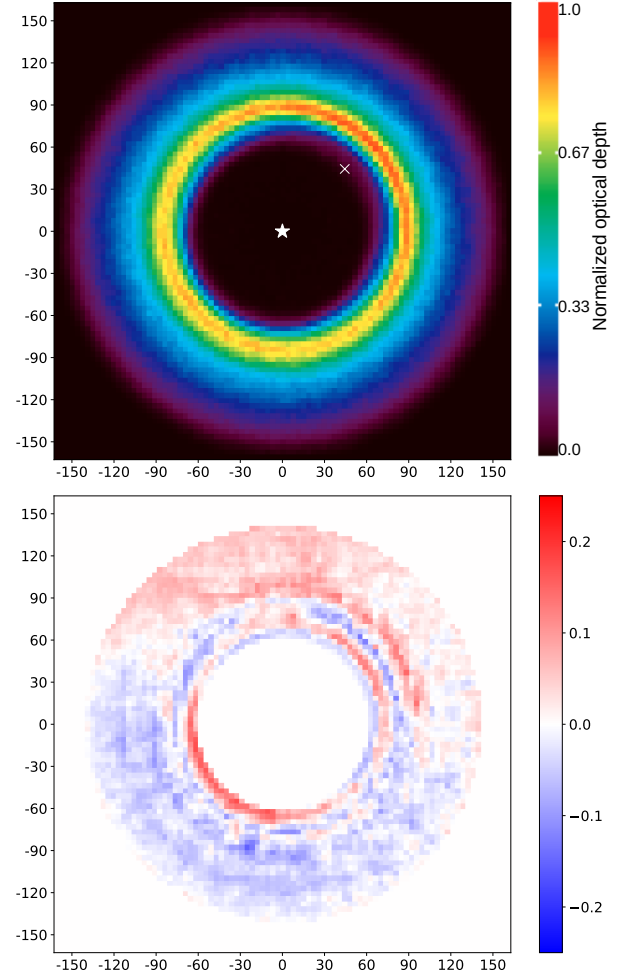
3.5 Behaviour of Larger Particles

Our Bayesian searches attempted to fit particles of $\beta = 0.4$ to 0.6 , (particle radii of $1 - 2 \mu\text{m}$ for mean grain density of 2 g/cm^3). Such small particles are observable in the visible bandpass of STIS, but would be less prominent or invisible at longer wavelengths. The fact that observations at different wavelengths are sensitive to different particle sizes may provide an explanation of why observations of HD 181327 in the infrared by Milli, J. et al. (2024) and at millimeter wavelengths by Marino et al. (2016) both indicated an axisymmetric disk without a pronounced arc such as reported by Stark et al. (2014).

To examine whether larger particles might not be driven to an asymmetry as pronounced as the smaller ones (as initially noted in Section 3.1), we took the best-fit planetary parameters from our 60 kyr collision lifetime result (Table 1) and applied it to an identically structured initial disk, but composed of larger particles with $\beta = 0.05$

Table 1. Posteriors and Best-Fit Results at Different Particle Lifetimes

Particle Lifetime	16 kyr	25 kyr	40 kyr	60 kyr	80 kyr	100 kyr	150 kyr	200 kyr
Posterior mass (M_J)	$5.22^{+0.86}_{-1.34}$	$4.61^{+1.49}_{-1.64}$	$4.64^{+1.46}_{-1.55}$	$4.34^{+1.75}_{-1.68}$	$4.09^{+1.94}_{-1.80}$	$4.01^{+2.01}_{-1.70}$	$3.39^{+2.46}_{-1.43}$	$2.83^{+2.25}_{-1.08}$
Posterior semimajor axis (au)	$61.68^{+0.84}_{-0.65}$	$61.84^{+1.19}_{-1.28}$	$61.61^{+0.98}_{-1.28}$	$61.81^{+1.11}_{-1.43}$	$61.91^{+1.55}_{-1.11}$	$62.02^{+1.58}_{-1.38}$	$62.55^{+1.25}_{-1.88}$	$63.03^{+1.07}_{-1.57}$
Best fit mass (M_J)	5.28	3.99	3.77	3.41	3.17	2.76	2.69	2.22
Best fit semimajor axis (au)	61.60	62.54	62.06	62.27	62.55	62.85	62.83	63.47
χ^2 per pixel of complete map	0.102	0.096	0.093	0.094	0.096	0.099	0.101	0.100
Maximum Target - Simulation	0.171	0.193	0.157	0.161	0.167	0.180	0.173	0.186

**Figure 4.** Best Fit result for a particle lifespan of 60 kyr. The top image is the optical depth map, while the bottom is the difference map (target values minus simulated values).**Figure 5.** Best Fit result for a particle lifespan of 150 kyr. The top image is the optical depth map, while the bottom is the difference map (target values minus simulated values).

to 0.2 (grain sizes of $14\mu\text{m}$ to $3.5\mu\text{m}$). The resultant disk is shown in Figure 8. This disk shows no pileup of particles in an arc near the planet. The overall optical depth distribution is largely azimuthally symmetric. We also attempt this for other particle lifespans, and find the same result: the larger, low- β particles are not being driven into an arc of high density over the timescales we consider here.

We also searched for a set of planetary parameters that could drive these larger particles into a similar arc. We ran MultiNest using particles with low β values, from 0.001 to 0.1 (particles of size $\sim 700\mu\text{m}$ to $\sim 7\mu\text{m}$ respectively). Our best results were again unable

to find a good match to the Target Map, even with a lifetime as long 100 kyr. The best-fit was from a planet of $1.5 M_J$ at a distance of 62 au, but while this configuration creates the primary central ring, it does not produce a focused 90° arc. The resultant map is shown in Figure 9.

For HD 181327, the planet that is capable of creating a 90° arc using $\beta \approx 0.5$ particles is unable to do so for particles of $\beta < 0.2$ particles. Also, a Bayesian search using exclusively $\beta < 0.1$ particles was unable to find a solution that matched the Target Disk. Therefore, the presence of particles of different sizes within the disk may explain

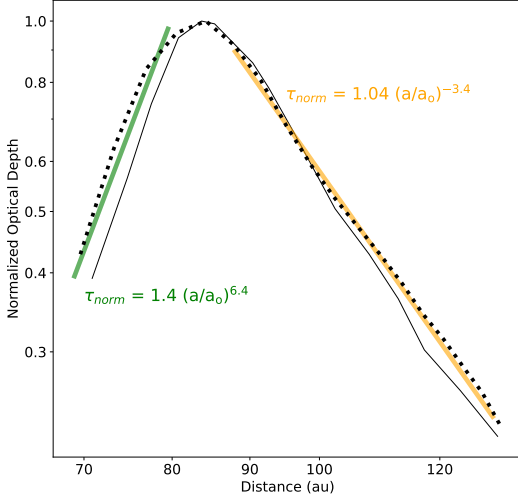


Figure 6. Normalized mean optical depth profile of the disk. The dotted line is our simulated result for the 60 kyr lifespan (see Table 1), with the best-fit lines for our data shown in red and yellow. The slopes of the optical depth from 65 to 80 au and from 90 to 130 au closely match the slopes found in Stark et al. (2014), which we recreate here with the solid black line.

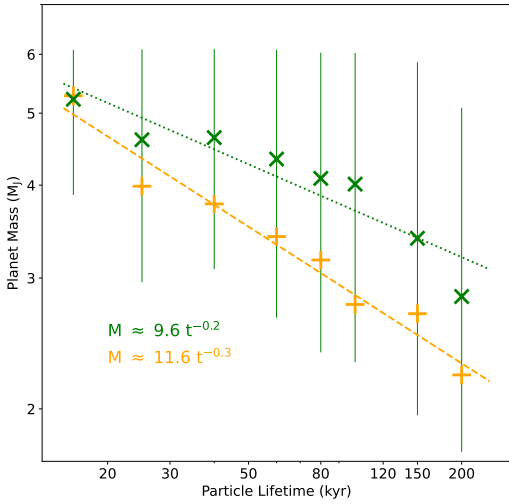


Figure 7. The green dotted line indicates the posterior masses with 1σ error bars as a function of particle lifetime. The orange dashed line shows the best-fit masses as a function of particle time. (t is in kyr, and resultant mass in Jupiter masses.)

not just the asymmetry seen in visible observations, but also the lack of asymmetry seen at longer wavelengths by Milli, J. et al. (2024) and Marino et al. (2016). The longer wavelength observations cannot see the asymmetry because the small particles responsible for the asymmetry are largely invisible to those longer wavelengths.

3.6 Detection Limits of Planet Masses

There have been previous estimates and limits placed on the mass and orbital distance of a potential planet within the HD 181327 system. As part of the Gemini NICI planet-finding campaign (using direct imaging), Wahhaj et al. (2013) estimated that a $4.0 M_J$ in HD 181324 would be detectable at $1.0''$ from the central star and a $2.6 M_J$ planet at $2.0''$. Interpolating from their limits, the detectability

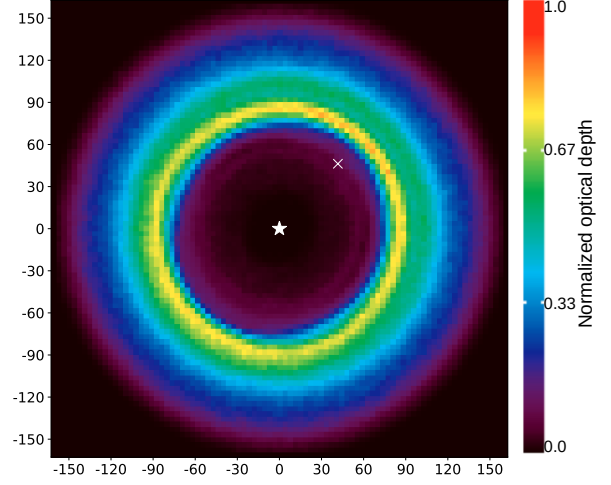


Figure 8. Behaviour of larger particles, $\beta=0.0-0.2$, under the influence of the Best Fit planet with the 60 kyr lifespan from Table 1. The disk is mostly axisymmetric, and does not show an arc of 90° .

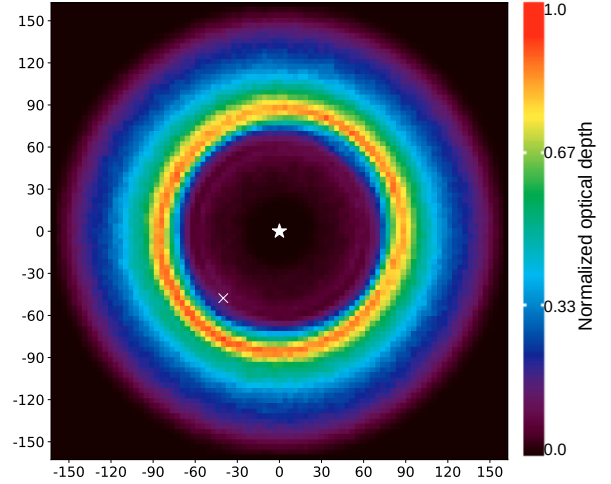


Figure 9. Best-Fit result of our MultiNest search using particles of $\beta=0.001-0.1$ with lifetime of 100 kyr. The peak density shows some variations angularly, but there is no focused arc of 90° .

our best-fit planetary distance (62 au , or $1.3''$) would be $\sim 3.5 M_J$. This suggests that our predicted planet must have a mass lower than $3.5 M_J$, otherwise the Gemini NICI campaign would have observed it.

In another study, Rodigas et al. (2014) through dynamical N-body simulations made predictions for shepherding planets in the interior of several debris disks. For HD 181327, they found the planet could have a mass no larger than $15 M_J$ and must be at least 35 au from the star, and our results are consistent with these limits.

Our simulations point to a planet with a semimajor axis of $\approx 62 \text{ au}$ and a range of possible masses, 2.8 to $4.6 M_J$ depending on particle lifetime. While our posteriors are well inside of the limits set by Rodigas et al. (2014), our posterior planet masses are typically above the values set by Wahhaj et al. (2013), though within the uncertainties. However, our MultiNest results indicate that quality of fit is not very sensitive to the planet mass, with 1σ errors of typically 40% . There are many simulations with a significantly lower-mass planet that produce results comparable to the best fit results shown in Table 1. In

fact, our best-fit masses are always lower than the nominal posterior values. Further, for particle lifetimes of 60+ kyr our best-fit values are all below the Wahhaj limit. At most timescales, one can find quality solutions that recreate the observed arc, while still adhering to previously established limitations. Thus, our results are consistent with both [Wahhaj et al. \(2013\)](#) and [Rodigas et al. \(2014\)](#).

4 SUMMARY

The primary goal of this study was to determine whether a planet could be the cause of the asymmetry in the HD 181327 debris disk reported by [Stark et al. \(2014\)](#), and if so to parameterize such a planet. We find that a planet can indeed reproduce the observed arc. We summarize the relevant requirements and results below.

- Grains are produced throughout the disk from an exo-Kuiper belt with a production density profile that decays as $a^{-3.25}$.
- The lifetime of micron-sized grains is at least 20 kyr.
- Contributing grains are initially released onto low-eccentricity orbits (implying energetic processes). Grains released onto high eccentricity orbits are either lost quickly or on such large orbits that they do not interact much with the planet.
- The planet has a mass of 2-5M_J and semimajor axis of 61-64 au.
- The longer the grains' expected lifetime, the smaller the mass of planet required to produce the arc.
- Only grains with $\beta \approx 0.5$ are quickly driven to the requisite pattern. This may explain why the arc is reported at visible wavelengths but is not at longer wavelengths.

The structure of the HD-181327 disk as observed by Stark et al. is easily reproducible by the presence of a garden-variety giant planet within the system. The hypothesis can also explain the absence of structure seen at longer wavelengths, as larger particles do not take on the same distinct arc as seen at smaller particles. The match to the disk structure and cross-section of the resulting disk is good enough that we predict that a planet will be detected in the system as observational techniques improve, and predict that it will be found along the line joining the star to the densest concentration of the arc. We encourage further observations of the system to corroborate or refute this prediction.

5 ACKNOWLEDGEMENTS

This work was funded in part by the Natural Sciences and Engineering Research Council of Canada Discovery Grants program (Grant no. RGPIN-2024-05200).

6 DATA AVAILABILITY

This paper is based on the work of [Stark et al. \(2014\)](#), and all source data comes directly from that work. No new data were generated in support of this research.

REFERENCES

- Augereau J. C., Nelson R. P., Lagrange A. M., Papaloizou J. C. B., Mouillet D., 2001, *A&A*, **370**, 447
 Feroz F., Hobson M. P., Bridges M., 2009, *MNRAS*, **398**, 1601
 Gaia Collaboration et al., 2018, *A&A*, **616**, A1

- Jutzi M., Michel P., Richardson D. C., 2019, *Icarus*, **317**, 215
 Kraus S., et al., 2013, *The Astrophysical Journal*, **768**, 80
 Lebreton J., et al., 2012, *A&A*, **539**, A17
 Marino S., et al., 2016, *MNRAS*, **460**, 2933
 Medallon S. C., Rickman E. F., Brown J., 2023, Technical report, STIS Instrument Handbook, <https://hst-docs.stsci.edu/stisihb>. STScI, Baltimore, <https://hst-docs.stsci.edu/stisihb>
 Milli, J. et al., 2024, *A&A*, **683**, A22
 Miret-Roig N., et al., 2020, *A&A*, **642**, A179
 Mouillet D., Larwood J. D., Papaloizou J. C. B., Lagrange A. M., 1997, *Monthly Notices of the Royal Astronomical Society*, **292**, 896
 Rodigas T. J., Malhotra R., Hinz P. M., 2014, *The Astrophysical Journal*, **780**, 65
 Schneider G., et al., 2006, *ApJ*, **650**, 414
 Schneider G., et al., 2014, *The Astronomical Journal*, **148**, 59
 Stark C. C., Schneider G., Weinberger A. J., Debes J. H., Grady C. A., Jang-Condell H., Kuchner M. J., 2014, *ApJ*, **789**, 58
 Tabeshian M., Wiegert P. A., 2016, *ApJ*, **818**, 159
 Tabeshian M., Wiegert P. A., 2017, *ApJ*, **847**, 24
 Tabeshian M., Wiegert P. A., 2018, *ApJ*, **857**, 3
 Thébaud P., Augereau J. C., 2007, *A&A*, **472**, 169
 Wahhaj Z., et al., 2013, *ApJ*, **773**, 179
 Wisdom J., Holman M., 1991, *AJ*, **102**, 1528
 Wyatt S. P., Whipple F. L., 1950, *The Astrophysical Journal*, **111**, 134
 Wyatt M. C., Dermott S. F., Telesco C. M., Fisher R. S., Grogan K., Holmes E. K., Piña R. K., 1999, *ApJ*, **527**, 918
 van de Hulst H. C., 1957, *Light Scattering by Small Particles*. Wiley, New York

This paper has been typeset from a $\text{\TeX}/\text{\LaTeX}$ file prepared by the author.